

# Chemical Science

Accepted Manuscript

This article can be cited before page numbers have been issued, to do this please use: W. Li, J. Ren, W. Guo, Q. Guo, S. Zhang and Y. Qu, *Chem. Sci.*, 2026, DOI: 10.1039/D6SC03014A.



This is an Accepted Manuscript, which has been through the Royal Society of Chemistry peer review process and has been accepted for publication.

Accepted Manuscripts are published online shortly after acceptance, before technical editing, formatting and proof reading. Using this free service, authors can make their results available to the community, in citable form, before we publish the edited article. We will replace this Accepted Manuscript with the edited and formatted Advance Article as soon as it is available.

You can find more information about Accepted Manuscripts in the [Information for Authors](#).

Please note that technical editing may introduce minor changes to the text and/or graphics, which may alter content. The journal's standard [Terms & Conditions](#) and the [Ethical guidelines](#) still apply. In no event shall the Royal Society of Chemistry be held responsible for any errors or omissions in this Accepted Manuscript or any consequences arising from the use of any information it contains.

## ARTICLE

**Spatial decoupling of CH<sub>4</sub> oxidation and CO<sub>2</sub> reduction enables near-stoichiometric dry reforming of methane**Wenbin Li,<sup>a</sup> Jiyun Ren,<sup>a</sup> Wenjie Guo,<sup>a</sup> Qing Guo,<sup>a</sup> Sai Zhang<sup>a,\*</sup> and Yongquan Qu<sup>a,\*</sup>Received 00th January 20xx,  
Accepted 00th January 20xx

DOI: 10.1039/x0xx00000x

The practical application of dry reforming of methane (DRM) is hindered by catalyst deactivation, primarily due to the deviation of the ideal 1:1 H<sub>2</sub>:CO stoichiometry for competitive CH<sub>4</sub> and CO<sub>2</sub> adsorption/activation. Excessive CH<sub>4</sub> decomposition results in H<sub>2</sub>:CO > 1 with carbon deposition, while predominant CO<sub>2</sub> chemisorption leads to H<sub>2</sub>:CO < 1 with favorable reverse water-gas shift (RWGS) side reaction. Herein, we demonstrate an \*O-migration coupling strategy on Pt/CeO<sub>2</sub> featuring Pt clusters and frustrated Lewis pairs (FLP, consisting of two Ce<sup>3+</sup> and one lattice oxygen) to achieve near-stoichiometric and durable DRM. The FLP sites on the CeO<sub>2</sub> support, independent of Pt-CeO<sub>2</sub> interfaces, reduce CO<sub>2</sub> to CO while generating \*O species. These \*O species migrate to Pt clusters, driving the partial CH<sub>4</sub> oxidation. Through this \*O-migration-enabled spatial decoupling of CO<sub>2</sub> reduction and CH<sub>4</sub> oxidation, the catalyst delivers a near-stoichiometric H<sub>2</sub>:CO ratio of 0.99 and an unprecedented CH<sub>4</sub> conversion rate of 93.9 mol g<sub>Pt</sub><sup>-1</sup> h<sup>-1</sup> at 700 °C. Moreover, stable performance is maintained for over 400 h, with a turnover number exceeding 7,200,000. This work establishes oxygen migration coupling as a potential strategy for spatially decoupled redox catalysis beyond DRM.

**Introduction**

Syngas (CO/H<sub>2</sub>), a pivotal platform for chemical synthesis, is projected to reach a global production capacity exceeding 290.9 million Nm<sup>3</sup>/hr in 2025.<sup>1</sup> Dry reforming of methane (DRM) represents a particularly promising route for syngas production, offering the dual advantages of reducing carbon emissions and supplying valuable feedstock.<sup>2-6</sup> However, on conventional catalysts, competitive adsorption/activation of CH<sub>4</sub> and CO<sub>2</sub> at catalyst surface invariably lead to preferential conversion of one reactant, deviating the H<sub>2</sub>:CO ratio from unity.<sup>7-11</sup> As illustration in Figure 1a, excessive CH<sub>4</sub> adsorption and decomposition lead to elevated H<sub>2</sub>:CO ratios (>1) and severe carbon deposition, causing catalyst deactivation.<sup>7, 12, 13</sup> Conversely, predominant CO<sub>2</sub> chemisorption triggers the reverse water-gas shift (RWGS) reaction, resulting in sub-stoichiometric H<sub>2</sub>:CO ratios (<1) and compromised hydrogen utilization.<sup>11, 14-17</sup> Therefore, the rational design of catalysts that can balance CH<sub>4</sub> and CO<sub>2</sub> activation is essential to realize near-stoichiometric DRM, further enabling the unlock durable, and industrial-scale application.

A temporal decoupling strategy, chemical looping DRM, has been advanced to address competitive adsorption by separating CH<sub>4</sub> oxidation and CO<sub>2</sub> reduction into alternating steps over oxygen-storage materials (Figure 1b).<sup>18-20</sup> This approach effectively suppresses coking formation and avoids RWGS, enabling near-stoichiometric H<sub>2</sub>:CO ratios (~1). Despite this promise, the practical

implementation of chemical looping DRM suffers from inherent drawbacks, including energy-intensive temperature swings, reliance on inert gas purging for phase separation, and sluggish kinetics of oxygen mobility in oxygen storage materials, collectively hindering scalability and operational flexibility.

Herein, we report a rationally designed catalyst featuring dual-active sites of Pt clusters and frustrated Lewis pairs (FLP) (Figure 1c), where CH<sub>4</sub> oxidation and CO<sub>2</sub> reduction proceed concurrently yet remain spatially segregated on distinct catalytic sites, subsequently coupling through \*O migration across the CeO<sub>2</sub> support. The FLP sites on CeO<sub>2</sub>(110), composed of adjacent Ce<sup>3+</sup> Lewis acids paired with a neighbouring lattice O<sup>2-</sup> Lewis base (Figure 1c),<sup>21</sup> exhibit exceptional CO<sub>2</sub> adsorption and activation, outperforming conventional oxygen vacancies and metal-CeO<sub>2</sub> interfaces. This enables spatial decoupling of CO<sub>2</sub> reduction from CH<sub>4</sub> dissociation on Pt clusters. Mechanistically, CO<sub>2</sub> reduction at FLP sites directly generates CO and reactive \*O species; the \*O then migrates rapidly across the CeO<sub>2</sub> surface to Pt clusters, where it drives the partial oxidation of CH<sub>4</sub> to H<sub>2</sub> and CO (Figure 1c). This dynamic coupling affords a near-stoichiometric H<sub>2</sub>:CO ratio of 0.99, which in turn delivers exceptional catalytic stability (>400 h) with a turnover number exceeding 7,200,000. Moreover, the catalyst achieves a remarkable CH<sub>4</sub> conversion rate of 93.9 mol g<sub>Pt</sub><sup>-1</sup> h<sup>-1</sup> at 700 °C, surpassing recently reported state-of-the-art systems.

<sup>a</sup> School of Chemistry and Chemical Engineering, Northwestern Polytechnical University, 710072 Xi'an, China

\* Corresponding author: Email: [zhangsai1112@nwpu.edu.cn](mailto:zhangsai1112@nwpu.edu.cn) and [yongquan@nwpu.edu.cn](mailto:yongquan@nwpu.edu.cn)

Supplementary Information available: [details of any supplementary information available should be included here]. See DOI: 10.1039/x0xx00000x



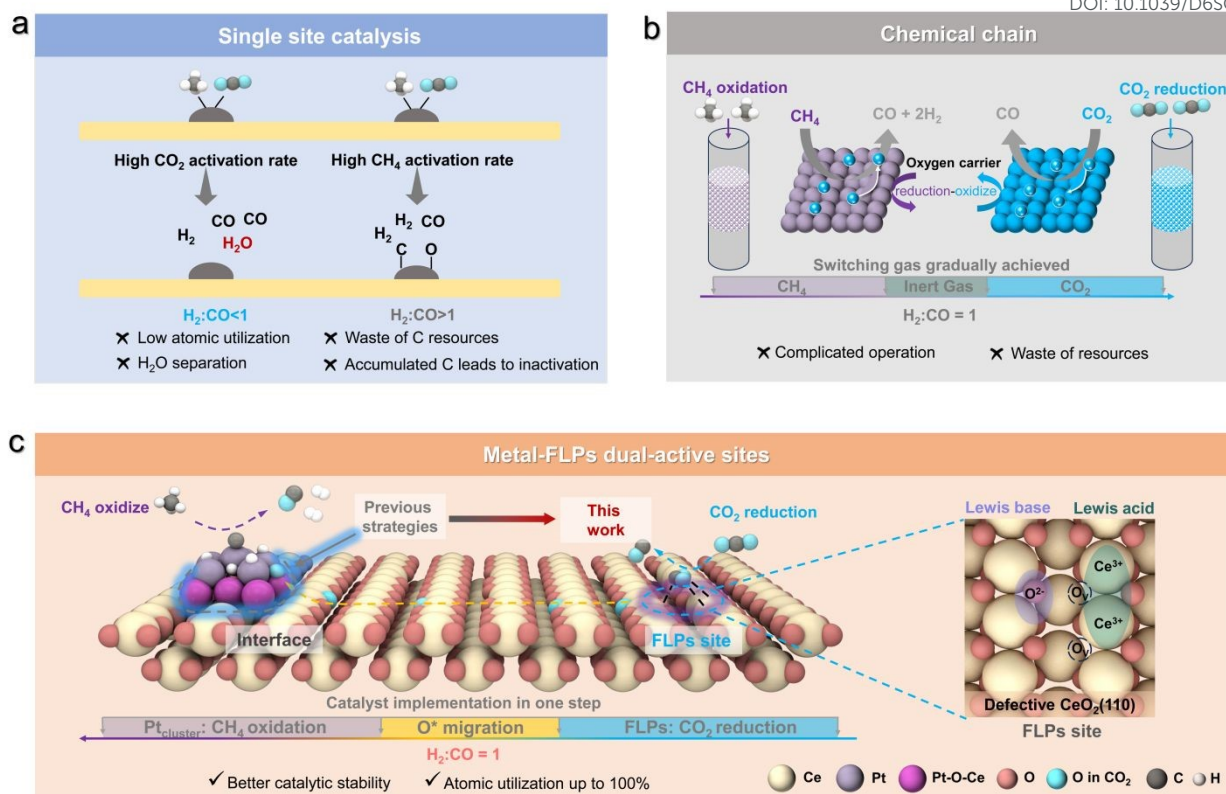


**Figure 1. Spatially decoupled  $\text{CO}_2$  reduction and  $\text{CH}_4$  oxidation.** (a) Schematic diagram highlighting the inherent limitations of conventional DRM catalysts. (b) Schematic diagram of Chemical looping DRM, achieving separation of  $\text{CO}_2$  reduction and  $\text{CH}_4$  oxidation. (c) Conceptual illustration of the spatially decoupled  $\text{CH}_4$  oxidation and  $\text{CO}_2$  reduction on the Pt clusters and FLPs sites, respectively, mediated through oxygen spillover.

## Results and discussion

**Theoretical investigation and catalytic performance.** Ceria ( $\text{CeO}_2$ ) serves as an ideal oxygen storage component owing to its exceptional redox properties and defect-engineered surface chemistry, which facilitates facile oxygen mobility within its lattice.<sup>22–24</sup> However, the nonpolar C-H bonds of  $\text{CH}_4$  resist activation on the Lewis acid/base pairs of  $\text{CeO}_2$ , necessitating metal sites where  $d$ -orbitals facilitate the requisite electron transfer for C-H scission.<sup>17, 25–28</sup> In contrast,  $\text{CO}_2$  adsorption is efficiently promoted at the metal- $\text{CeO}_2$  interface.<sup>29–31</sup> To achieve spatially decoupled catalysis, we reasoned that the  $\text{CeO}_2$  supports must possess sites with exceptionally strong and selective affinity for  $\text{CO}_2$ , thereby isolating its activation from  $\text{CH}_4$  oxidation on metal sites and preventing  $^* \text{H}$  intermediates from triggering the deleterious RWGS reaction.

Density functional theory (DFT) calculations were employed to guide this design. As shown in Figure 2a and S1–S5,  $\text{CO}_2$  adsorption at oxygen vacancy ( $\text{O}_v$ ) on  $\text{CeO}_2(110)$  ( $\text{CeO}_2(110)\text{-O}_v$ ) is significantly stronger than that on  $\text{CeO}_2(111)\text{-O}_v$ , with an adsorption energy of  $-2.51$  eV. Although this value is more negative than that for  $\text{CO}_2$  adsorption on  $\text{Pt}_6$  clusters, it remains comparable to that at the  $\text{Pt}_6\text{-CeO}_2$  interface, indicating that isolated  $\text{O}_v$  is insufficient to achieve the full spatial decoupling. Notably, constructing adjacent  $\text{O}_v$  pairs on  $\text{CeO}_2(110)$  creates the FLP sites ( $\text{Ce}^{3+}\dots\text{Ce}^{3+}, \text{O}^{2-}$ ; Figure 2b), which dramatically enhance  $\text{CO}_2$  adsorption, with an energy of  $-3.30$  eV

(Figure 2a). In contrast, creating more  $\text{O}_v$  on  $\text{CeO}_2(111)$  merely increases the number of  $\text{O}_v$  without creating a distinct adsorption site (Figure 2b). These results confirm that FLP on  $\text{CeO}_2(110)$ , coupled with Pt clusters, provides an ideal platform for spatially decoupled catalysis toward efficient and stoichiometric DRM.

Guided by the above analysis, we synthesized porous  $\text{CeO}_2$  nanorods (denoted as  $\text{CeO}_2\text{-FLP}$ ) designed to host FLP sites through a sequential low- and high-pressure hydrothermal method.<sup>21, 32</sup> Dark-field transmission electron microscopy (TEM) images revealed a well-defined porous architecture with an average pore size of  $2\sim 3$  nm (Figure S6a). High-resolution TEM showed lattice fringes with a lattice fringe spacing of  $0.19$  nm, corresponding to the  $\text{CeO}_2$  [220] planes (Figure S6b), indicating the preferential growth along the [110] direction. X-ray photoelectron spectroscopy (XPS) analysis of Ce 3d and O 1s peaks indicated the abundance of surface defects in  $\text{CeO}_2\text{-FLP}$ , as evidenced by the  $\text{Ce}^{3+}$  (29.4%, Figure S7a) and  $\text{Ce}^{3+}\text{-O}$  (52.4%, Figure S7b) fractions. The abundance of  $\text{O}_v$ , along with the exposure of (110) facets, suggests the effective formation of FLP sites on the  $\text{CeO}_2\text{-FLP}$  surface.<sup>21, 33, 34</sup>

Subsequently, Pt clusters were deposited on  $\text{CeO}_2\text{-FLP}$  ( $\text{Pt}_{\text{cluster}}/\text{CeO}_2\text{-FLP}$ ) using  $\text{H}_2\text{PtCl}_6\cdot 6\text{H}_2\text{O}$  as precursors *via* a photo-assisted reduction process. The actual Pt loading was quantified to be  $0.9$  wt.% using inductively coupled plasma optical emission spectroscopy (ICP-OES). High-angle annular dark-field scanning transmission electron microscopy (HAADF-STEM) images of



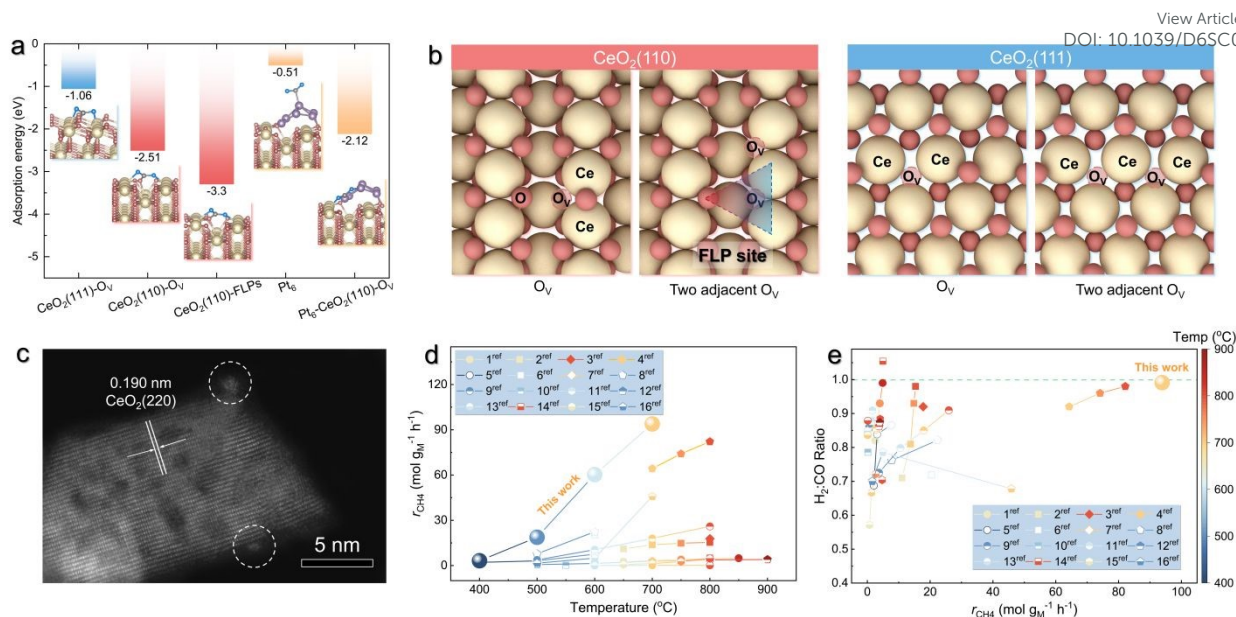


**Figure 2. Theoretical investigation and catalytic performance.** (a) The CO<sub>2</sub> adsorption behaviors on the CeO<sub>2</sub>(110) surface with various active sites. (b) Optimized structure of one O<sub>v</sub> and two adjacent O<sub>v</sub>s on CeO<sub>2</sub>(110) and CeO<sub>2</sub>(111) surface. (c) HAADF-STEM image of Pt<sub>cluster</sub>/CeO<sub>2</sub>-FLP. (d) Comparison of CH<sub>4</sub> conversion rates over Pt<sub>cluster</sub>/CeO<sub>2</sub>-FLP and other state-of-the-art catalysts (See Table S2 for more details). (e) Comparison of CH<sub>4</sub> conversion rates and H<sub>2</sub>:CO ratios over Pt<sub>cluster</sub>/CeO<sub>2</sub>-FLP and other state-of-the-art catalysts under similar reaction conditions (See Table S2 for more details).

Pt<sub>cluster</sub>/CeO<sub>2</sub>-FLP revealed brightness variation on CeO<sub>2</sub>-FLP (Figure 2c), indicating the presence of Pt clusters with an average size of 0.9 ± 0.1 nm (Figure S8). CO chemical adsorption determined a Pt dispersion of 43.2% (Table S1). Importantly, Pt<sub>cluster</sub>/CeO<sub>2</sub>-FLP retained high Ce<sup>3+</sup> (30.9%) and Ce<sup>3+</sup>-O (55.2%) fractions (Figure S7), confirming the preservation of the FLP-rich surface.

The DRM performances of Pt<sub>cluster</sub>/CeO<sub>2</sub>-FLP were evaluated in a fixed-bed reactor under a feed of CH<sub>4</sub>:CO<sub>2</sub>:N<sub>2</sub> (2:2:1). At 700 °C, Pt<sub>cluster</sub>/CeO<sub>2</sub>-FLP achieved a CH<sub>4</sub> conversion of 75.7% (Figure S9), approaching the thermodynamic equilibrium (76.0%, at 700 °C), along with a CH<sub>4</sub> conversion rate of 93.9 mol g<sub>Pt</sub><sup>-1</sup> h<sup>-1</sup>. This activity substantially exceeds that of state-of-the-art catalysts (Figure 2d and Table S2). Importantly, the H<sub>2</sub> and CO production rates reached 187.7 mol g<sub>Pt</sub><sup>-1</sup> h<sup>-1</sup> and 189.5 mol g<sub>Pt</sub><sup>-1</sup> h<sup>-1</sup>, respectively, giving a near-stoichiometric H<sub>2</sub>:CO ratio of 0.99. Therefore, Pt<sub>cluster</sub>/CeO<sub>2</sub>-FLP delivers an unprecedented combination of high activity and ideal product stoichiometry for DRM (Figure 2e and Table S2).

**Critical functions of the FLP sites.** As catalyst design concept (Figure 1c), the FLP sites on the CeO<sub>2</sub>(110) surface, rather than Pt clusters or Pt-CeO<sub>2</sub> interfaces, are responsible for the strong CO<sub>2</sub> adsorption and activation. This capability is absent on CeO<sub>2</sub>(111) facet, theoretically leading to inferior DRM performance. We synthesized nano-octahedral CeO<sub>2</sub> (denoted as CeO<sub>2</sub>-O<sub>v</sub>) exclusively exposing (111) facets, which are structurally incompatible with FLP formation and thus possess only conventional O<sub>v</sub> (Figure 2b and S10).<sup>21</sup> Consistent with this morphology, CeO<sub>2</sub>-O<sub>v</sub> exhibited a lower concentration of surface defects, with Ce<sup>3+</sup> and Ce<sup>3+</sup>-O<sub>v</sub> fractions of 19.3% and 40.3%, respectively (Figure S11 and Table S1). Using the same photo-assisted deposition method, Pt clusters were loaded onto CeO<sub>2</sub>-O<sub>v</sub> (Pt<sub>cluster</sub>/CeO<sub>2</sub>-O<sub>v</sub>) at 1.1 wt.% loading. HAADF-STEM image confirmed the Pt clusters with an average size of 0.9 ± 0.3 nm

(Figure 3a and S12). Meanwhile, Pt deposition did not substantially alter the surface defect of CeO<sub>2</sub>-O<sub>v</sub>, with Ce<sup>3+</sup> and Ce<sup>3+</sup>-O fractions remaining at 20.4% and 42.4%, respectively (Figure S11 and Table S1). Under identical reaction conditions, Pt<sub>cluster</sub>/CeO<sub>2</sub>-O<sub>v</sub>, despite possessing comparable Pt clusters, exhibited markedly inferior DRM performance. Specifically, CH<sub>4</sub> conversion was 35.1% (Figure 3b), 2.2-fold lower than that of Pt<sub>cluster</sub>/CeO<sub>2</sub>-FLP (75.7%) at 700 °C. Meanwhile, the H<sub>2</sub>:CO ratio plummeted to 0.5, indicating severe deviation from stoichiometric product ratios (Figure 3b). These comparative results unequivocally establish that the FLP sites are essential for achieving exceptional DRM activity and stoichiometry.

Kinetic analysis at low conversions (<20%) further elucidates the critical role of FLP. The CO<sub>2</sub> reaction order over Pt<sub>cluster</sub>/CeO<sub>2</sub>-FLP was significantly lower than that over Pt<sub>cluster</sub>/CeO<sub>2</sub>-O<sub>v</sub> (Figure 3c), indicating higher CO<sub>2</sub> surface coverage on the FLP-containing catalyst. Arrhenius plots (Ln *k* vs. 1/*T*, Figure S13 and S14) revealed that the activation energy (*E<sub>a</sub>*) for CO<sub>2</sub> conversion on CeO<sub>2</sub>-FLP (59.6 kJ mol<sup>-1</sup>) was substantially lower than on CeO<sub>2</sub>-O<sub>v</sub> (79.1 kJ mol<sup>-1</sup>). Thus, the higher CO<sub>2</sub> coverage on Pt<sub>cluster</sub>/CeO<sub>2</sub> results in the stronger conversion capacity, directly distinguishing FLP from O<sub>v</sub>. This trend was further supported by CO<sub>2</sub> temperature-programmed desorption (CO<sub>2</sub>-TPD, Figure S15), in which CeO<sub>2</sub>-FLP displayed an additional strong desorption peak at ~500 °C, confirming enhanced CO<sub>2</sub> adsorption at the FLP sites.

More importantly, introducing Pt clusters onto CeO<sub>2</sub>-O<sub>v</sub> significantly reduced the *E<sub>a</sub>* for CO<sub>2</sub> conversion from 79.1 kJ mol<sup>-1</sup> (CeO<sub>2</sub>-O<sub>v</sub>) to 71.5 kJ mol<sup>-1</sup> (Pt<sub>cluster</sub>/CeO<sub>2</sub>-O<sub>v</sub>, Figure S14). In the absence of FLP sites on CeO<sub>2</sub> supports, CO<sub>2</sub> adsorption and activation are influenced by Pt or the Pt-CeO<sub>2</sub> interface, consistent with previous reports. Conversely, depositing Pt onto CeO<sub>2</sub>-FLP exhibited a negligible effect on the *E<sub>a</sub>* for CO<sub>2</sub> conversion, as evidenced by the



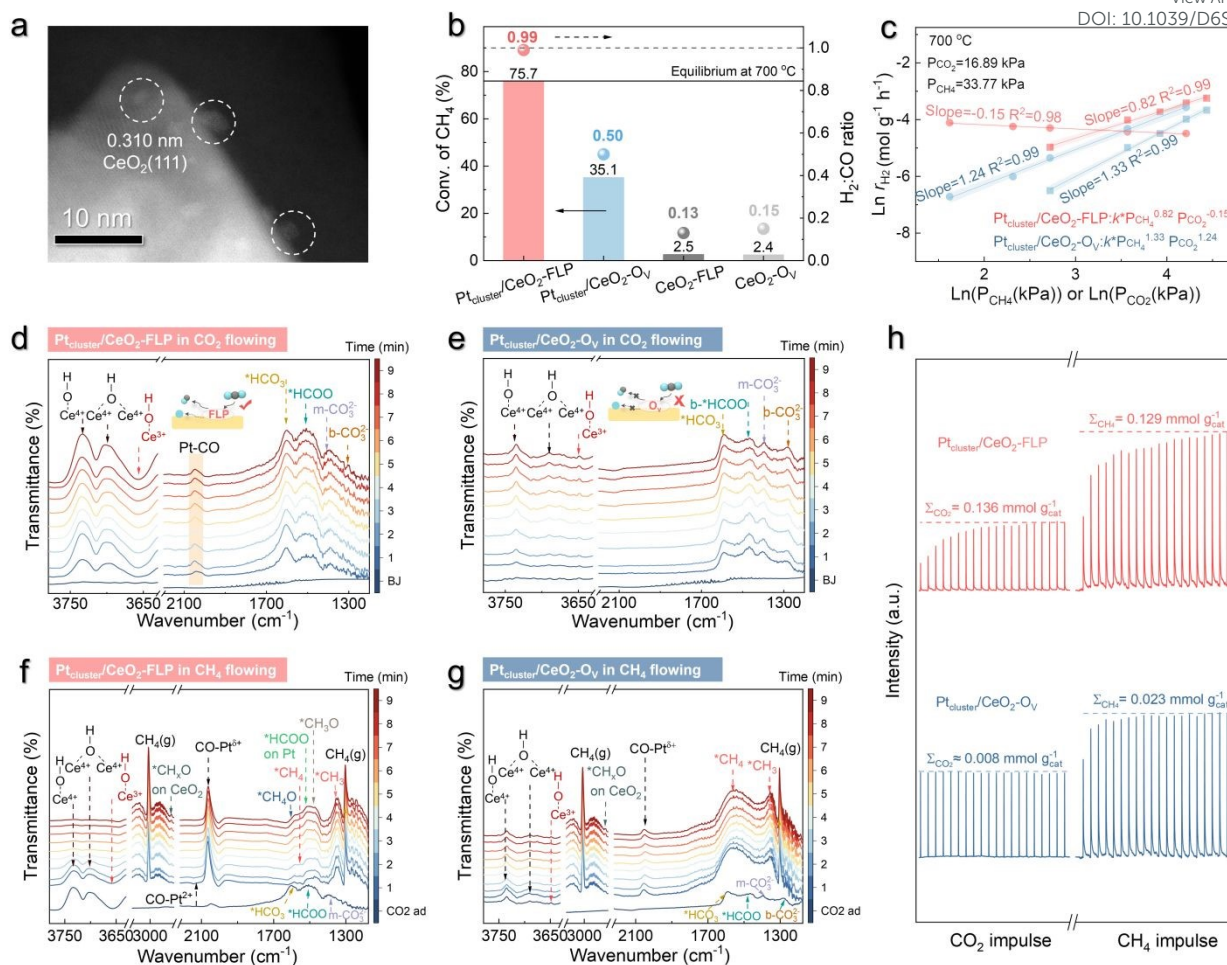


**Figure 3. Investigations on the critical functions of FLP.** (a) HAADF-STEM image of  $\text{Pt}_{\text{cluster}}/\text{CeO}_2\text{-O}_v$ . (b)  $\text{CH}_4$  conversions and  $\text{H}_2/\text{CO}$  ratios at  $700^\circ\text{C}$  with a WHSV of  $30,000 \text{ mL g}_{\text{cat}}^{-1} \text{ h}^{-1}$ . (c) Kinetic measurements of  $\text{Pt}_{\text{cluster}}/\text{CeO}_2\text{-FLP}$  and  $\text{Pt}_{\text{cluster}}/\text{CeO}_2\text{-O}_v$ . *In situ* DRIFTS spectra of (d)  $\text{Pt}_{\text{cluster}}/\text{CeO}_2\text{-FLP}$  and (e)  $\text{Pt}_{\text{cluster}}/\text{CeO}_2\text{-O}_v$  under  $\text{CO}_2$  flow. *In situ* DRIFTS spectra of (f)  $\text{Pt}_{\text{cluster}}/\text{CeO}_2\text{-FLP}$  and (g)  $\text{Pt}_{\text{cluster}}/\text{CeO}_2\text{-O}_v$  under  $\text{CH}_4$  flow after  $\text{CO}_2$  flow. **Note:** All of catalysts were pre-treated by Ar flow for 30 min. Initially, a flow of 50 vol.%  $\text{CO}_2/\text{Ar}$  was introduced and the DRIFTS signals were collected at  $350^\circ\text{C}$  every 1 min. Subsequently, the 50 vol.%  $\text{CO}_2/\text{Ar}$  gas was switched to a flow of 50 vol.%  $\text{CH}_4/\text{Ar}$ . The DRIFTS signals were further collected at  $350^\circ\text{C}$  every 1 min. (h) Pulsed reactions of  $\text{CO}_2$  and  $\text{CH}_4$  over  $\text{Pt}_{\text{cluster}}/\text{CeO}_2\text{-FLP}$  and  $\text{Pt}_{\text{cluster}}/\text{CeO}_2\text{-O}_v$ .

nearly identical values for  $\text{Pt}_{\text{cluster}}/\text{CeO}_2\text{-FLP}$  ( $55.7 \text{ kJ mol}^{-1}$ ) and  $\text{CeO}_2\text{-FLP}$  ( $59.6 \text{ kJ mol}^{-1}$ ; Figure S14). Different from conventional  $\text{O}_v$  sites, these kinetic results experimentally demonstrate that  $\text{CO}_2$  activation occurs predominantly on FLP sites rather than at Pt clusters or the Pt-O-Ce interfaces, with Pt clusters playing a negligible direct role in  $\text{CO}_2$  transformation.

Subsequently, *in situ* diffuse reflectance infrared Fourier transform spectroscopy (DRIFTS) was employed to monitor the roles of FLP under reaction conditions. Both  $\text{Pt}_{\text{cluster}}/\text{CeO}_2\text{-FLP}$  (Figure 3d) and  $\text{Pt}_{\text{cluster}}/\text{CeO}_2\text{-O}_v$  (Figure 3e) exhibited characteristic vibrational signatures of bicarbonate ( $^*\text{HCO}_3$ , at  $1602 \text{ cm}^{-1}$ ) and formate ( $^*\text{HCOO}$ ,  $1505 \text{ cm}^{-1}$ ) intermediates, confirming the  $\text{CO}_2$  chemisorption on  $\text{CeO}_2$  supports.<sup>35, 36</sup> However,  $\text{Pt}_{\text{cluster}}/\text{CeO}_2\text{-FLP}$  exhibited strong capacity of transformation of  $\text{b-CO}_3^{2-}$ , as evidenced from their much weaker adsorption peaks at  $\sim 1300 \text{ cm}^{-1}$ . Furthermore,  $\text{Pt}_{\text{cluster}}/\text{CeO}_2\text{-FLP}$  displayed an obvious  $^*\text{CO}$  adsorption band ( $\sim 2046 \text{ cm}^{-1}$ ) associated with Pt clusters, which was not detected on  $\text{Pt}_{\text{cluster}}/\text{CeO}_2\text{-O}_v$ . This critical distinction confirms that  $\text{CeO}_2\text{-FLP}$  enable direct  $\text{CO}_2$ -to- $\text{CO}$

reduction pathway.<sup>37, 38</sup> Moreover, during  $\text{CO}_2$  exposure on  $\text{Pt}_{\text{cluster}}/\text{CeO}_2\text{-FLP}$ , the  $\text{Ce}^{3+}\text{-OH}$  stretching mode ( $\sim 3656 \text{ cm}^{-1}$ ) attenuated while  $\text{Ce}^{4+}\text{-OH}$  features ( $\sim 3733 \text{ cm}^{-1}$  and  $\sim 3698 \text{ cm}^{-1}$ ) intensified (Figure 3d and 3e),<sup>39-41</sup> indicating the accumulation of  $^*\text{O}$  species within the  $\text{CeO}_2\text{-FLP}$  lattice during the  $\text{CO}_2$ -to- $\text{CO}$  reduction, accompanied by the  $\text{Ce}^{3+}$ -to- $\text{Ce}^{4+}$  oxidation.

When a  $\text{CH}_4$  flow was introduced into the *in situ* reactor,  $\text{Pt}_{\text{cluster}}/\text{CeO}_2\text{-FLP}$  exhibited a significantly enhanced intensity of  $^*\text{CO}$  adsorption on Pt clusters, indicating the  $\text{CH}_4$  oxidation occurred on the Pt sites (Figure 3f). Meanwhile, the vibrational features corresponding to the  $^*\text{CH}_3$  ( $\sim 1342 \text{ cm}^{-1}$ ),  $^*\text{CH}_3\text{O}$  ( $\sim 1471 \text{ cm}^{-1}$ ),  $^*\text{CH}_4\text{O}$  ( $\sim 1583 \text{ cm}^{-1}$ ) and Pt-bound  $^*\text{HCOO}$  ( $\sim 1517 \text{ cm}^{-1}$ ) species emerged during  $\text{CH}_4$  flow, along with the disappearance of  $\text{CeO}_2$ -bound  $^*\text{HCOO}$  ( $\sim 1509 \text{ cm}^{-1}$ ) and  $^*\text{CO}_3^{2-}$  ( $\sim 1397 \text{ cm}^{-1}$ ) intermediates. Simultaneously, the  $\text{Ce}^{4+}$  species ( $\text{Ce}^{4+}\text{-OH}$ ,  $3733 \text{ cm}^{-1}$ ) was reduced to  $\text{Ce}^{3+}$  ( $\text{Ce}^{3+}\text{-OH}$ ,  $3658 \text{ cm}^{-1}$ ) along these transformations. Thus, these findings collectively demonstrate that  $\text{CH}_4$  oxidation is mediated by lattice  $^*\text{O}$  species originating from  $\text{CeO}_2\text{-FLP}$  supports.



In contrast, Pt<sub>cluster</sub>/CeO<sub>2</sub>-O<sub>v</sub> exhibited negligible activity for this reaction pathway (Figure 3g). The CH<sub>4</sub> exposure on Pt<sub>cluster</sub>/CeO<sub>2</sub>-O<sub>v</sub> induced the rapid emergence of \*CH<sub>3</sub> (at ~1342 cm<sup>-1</sup>) and \*CH<sub>4</sub> (at ~1557 cm<sup>-1</sup>) species, indicating CH<sub>4</sub> adsorption and activation occurred on Pt sites.<sup>42, 43</sup> However, CO production remained consistently low, demonstrating limited further oxidation of activated \*CH<sub>3</sub> and \*CH<sub>4</sub> species to \*CO. Furthermore, the partial retention of Ce<sup>4+</sup> species (Ce<sup>4+</sup>-OH, 3733 cm<sup>-1</sup>) indicated the restricted \*O migration during CH<sub>4</sub> flow, owing to the poor capacity for CO<sub>2</sub> activation/reduction of CeO<sub>2</sub>-O<sub>v</sub>. Concomitantly, the disappearance of \*HCO<sub>3</sub>, \*HCOO, and b-CO<sub>3</sub><sup>2-</sup> species could be attributed to the \*H spillover from Pt into the CeO<sub>2</sub>-O<sub>v</sub> supports.

Sequential CO<sub>2</sub>/CH<sub>4</sub> pulse experiments further quantified the FLP functions. Pt<sub>cluster</sub>/CeO<sub>2</sub>-FLP showed distinct CO<sub>2</sub> consumption over 14 pulse cycles, corresponding to an \*O storage capacity of 0.136 mmol g<sub>cat</sub><sup>-1</sup>. This observation contrasted sharply with Pt<sub>cluster</sub>/CeO<sub>2</sub>-O<sub>v</sub>, which exhibited a negligible \*O storage capacity (0.008 mmol g<sub>cat</sub><sup>-1</sup>), consistent with *in situ* DRIFTS spectra confirming only adsorption of CO<sub>2</sub> on CeO<sub>2</sub>-O<sub>v</sub> (Figure 3h). Subsequent CH<sub>4</sub> pulses revealed drastically higher consumption on Pt<sub>cluster</sub>/CeO<sub>2</sub>-FLP (0.129 mmol<sub>CH4</sub> g<sub>cat</sub><sup>-1</sup>) than that on Pt<sub>cluster</sub>/CeO<sub>2</sub>-O<sub>v</sub> (0.023 mmol<sub>CH4</sub> g<sub>cat</sub><sup>-1</sup>). The close match between CH<sub>4</sub> consumption and \*O storage on Pt<sub>cluster</sub>/CeO<sub>2</sub>-FLP confirms efficient transfer of the FLP-generated \*O species to Pt sites for CH<sub>4</sub> oxidation.

**Investigation on the functions of Pt clusters.** Notably, the pronounced reduction in *E<sub>a</sub>* for CH<sub>4</sub> conversion upon introducing Pt cluster (Pt<sub>cluster</sub>/CeO<sub>2</sub>-FLP and CeO<sub>2</sub>-FLP, 64.1 kJ mol<sup>-1</sup> and 112.6 kJ mol<sup>-1</sup>; Pt<sub>cluster</sub>/CeO<sub>2</sub>-O<sub>v</sub> and CeO<sub>2</sub>-O<sub>v</sub>, 79.2 kJ mol<sup>-1</sup> and 117.2 kJ mol<sup>-1</sup>; Figure S14) unambiguously underscores the essential roles of Pt in CH<sub>4</sub> adsorption and C-H bond activation. Moreover, the comparable CH<sub>4</sub> reaction orders observed on both Pt<sub>cluster</sub>/CeO<sub>2</sub>-FLP and Pt<sub>cluster</sub>/CeO<sub>2</sub>-O<sub>v</sub> indicated that CH<sub>4</sub> activation kinetics were weakly influenced by CeO<sub>2</sub> (Figure 3c). Taken together, the higher reaction orders and activation energies associated with CH<sub>4</sub> conversion indicated that CH<sub>4</sub> activation constitutes the rate-determining step in the DRM reaction over Pt<sub>cluster</sub>/CeO<sub>2</sub>-FLP, particularly under preconditions where CO<sub>2</sub> is efficiently activated by FLP.

To further decipher the mechanistic roles of Pt species in CH<sub>4</sub> activation, the single-atom Pt and Pt nanoparticles (average size 2.2 ± 0.1 nm) were deposited on CeO<sub>2</sub>-FLP, yielding Pt<sub>1</sub>/CeO<sub>2</sub>-FLP (Figure S16) and Pt<sub>NP</sub>/CeO<sub>2</sub>-FLP (Figure S17), respectively. ICP-OES determined Pt loadings of 0.5 wt.% for Pt<sub>1</sub>/CeO<sub>2</sub>-FLP and 1.0 wt.% for Pt<sub>NP</sub>/CeO<sub>2</sub>-FLP. Notably, the surface properties of the supports in Pt<sub>1</sub>/CeO<sub>2</sub>-FLP and Pt<sub>NP</sub>/CeO<sub>2</sub>-FLP were similar to those of Pt<sub>cluster</sub>/CeO<sub>2</sub>-FLP (Figure S18 and Table S1), enabling the systematic investigations of Pt speciation effects on CH<sub>4</sub> activation while excluding the influences of supports.

The Pt L<sub>3</sub> edge X-ray absorption near-edge structure (XANES) was used to investigate the electronic states of Pt. The white line peak of Pt<sub>1</sub>/CeO<sub>2</sub>-FLP located at 11567.4 eV, close to that of PtO<sub>2</sub> (Figure 4a). The *k*<sup>3</sup>-weight Fourier transforms of extended X-ray absorption fine structure (EXAFS) spectra of Pt<sub>1</sub>/CeO<sub>2</sub>-FLP delivered one prominent peak at ~1.64 Å, which was labeled as Pt-O bond (Figure 4b and S19). The lack of Pt-Pt coordination confirmed the atomically dispersed Pt supported on CeO<sub>2</sub>-FLP. The wavelet transform analysis directly revealed the absence of Pt-Pt bonds in Pt<sub>1</sub>/CeO<sub>2</sub>-FLP (Figure 4c). In contrast, Pt<sub>cluster</sub>/CeO<sub>2</sub>-FLP and Pt<sub>NP</sub>/CeO<sub>2</sub>-FLP exhibited the white

line peaks between Pt foil and PtO<sub>2</sub> (Figure 4a), indicating the mixed valence states of Pt. Meanwhile, both Pt-Pt and Pt-O bonds were clearly observed from the *k*<sup>3</sup>-weight Fourier transforms of EXAFS spectra. Compared to Pt<sub>NP</sub>/CeO<sub>2</sub>-FLP, the higher white line peak revealed the more amount of Pt-O bond in Pt<sub>cluster</sub>/CeO<sub>2</sub>-FLP, which could be clearly observed from the wavelet transform analysis. Quantitatively, Pt<sub>1</sub>/CeO<sub>2</sub>-FLP, Pt<sub>cluster</sub>/CeO<sub>2</sub>-FLP and Pt<sub>NP</sub>/CeO<sub>2</sub>-FLP exhibited the Pt-O fractions of 100%, 45.4% and 24.2%, as well as the Pt-Pt fractions of 0%, 54.6% and 75.8% (Table 1).

For the DRM reaction, Pt<sub>cluster</sub>/CeO<sub>2</sub>-FLP, featuring by the co-existence of Pt-O and Pt-Pt bonds, delivered the highest CH<sub>4</sub> conversion rate compared to Pt<sub>1</sub>/CeO<sub>2</sub>-FLP and Pt<sub>NP</sub>/CeO<sub>2</sub>-FLP (Figure 4d and S20), as well as the lowest *E<sub>a</sub>* of 64.1 kJ mol<sup>-1</sup> for CH<sub>4</sub> conversion (Figure 4e and S21). These observations confirm that the highest intrinsic activity of Pt clusters originates from a synergistic interplay between Pt-Pt and Pt-O bonds in CH<sub>4</sub> activation. This synergy arises from the presence of coordinatively unsaturated metal and oxygen on Pt surface, which promote the formation of the adsorbed CH<sub>4</sub> σ-complexes and then facilitate C-H bond cleavage in the complexes.<sup>25, 44</sup> Furthermore, due to their similar surface properties of supports, all Pt/CeO<sub>2</sub>-FLP catalysts exhibited the close *E<sub>a</sub>* values for CO<sub>2</sub> conversion (Figure 4e), further confirming the strong capacity of FLP for CO<sub>2</sub> adsorption/activation and the negligible influence of Pt active sites on this process.

The CH<sub>4</sub> activation on Pt/CeO<sub>2</sub>-FLP was further investigated by CH<sub>4</sub> temperature-programmed reduction (CH<sub>4</sub>-TPR). After the pre-treatment with Ar purging, a CH<sub>4</sub> flow was introduced to probe the catalyst surface. The CeO<sub>2</sub>-FLP supports alone exhibited no detectable activation peaks (Figure S22), further confirming that the CH<sub>4</sub> adsorption and activation occur exclusively at Pt sites. Importantly, Pt<sub>cluster</sub>/CeO<sub>2</sub>-FLP exhibited the strongest peak intensity and the lowest initiation temperature compared to both Pt<sub>1</sub>/CeO<sub>2</sub>-FLP and Pt<sub>NP</sub>/CeO<sub>2</sub>-FLP (Figure S22). These observations directly confirmed the highest capacity of Pt<sub>cluster</sub>/CeO<sub>2</sub>-FLP for the CH<sub>4</sub> adsorption and activation in DRM.

Subsequently, *in situ* DRIFTS experiments were performed to compare the behaviors of Pt clusters and nanoparticles under reaction conditions. Under CO<sub>2</sub> flow, Pt<sub>NP</sub>/CeO<sub>2</sub>-FLP exhibited spectral changes nearly identical to those of Pt<sub>cluster</sub>/CeO<sub>2</sub>-FLP, consistent with their similar CeO<sub>2</sub> surface properties for CO<sub>2</sub> adsorption (Figure 4f). Upon switching to CH<sub>4</sub> flow, characteristic peaks corresponding to adsorbed \*CH<sub>4</sub> (1557 cm<sup>-1</sup>) appeared on Pt<sub>NP</sub>/CeO<sub>2</sub>-FLP, confirming CH<sub>4</sub> adsorption (Figure 4g). Unlike Pt<sub>cluster</sub>/CeO<sub>2</sub>-FLP, no clear signals for \*CH<sub>x</sub>O intermediates were detected on Pt<sub>NP</sub>/CeO<sub>2</sub>-FLP. Moreover, the Ce<sup>4+</sup>-OH peak persisted even after 9 min CH<sub>4</sub> flow, indicating restricted \*O migration from the support to the Pt nanoparticles. Together with CH<sub>4</sub>-TPR results, these observations demonstrate that Pt clusters uniquely promote the migration of \*O species, which in turn enhances CH<sub>4</sub> activation and overall DRM activity.

Building on the foregoing analysis, the spatially separated Pt clusters and FLP sites serve distinct roles in CH<sub>4</sub> oxidation and CO<sub>2</sub> reduction, respectively, with \*O migration acting as the key coupling step, as illustrated in Figure 1c. To further probe the origin and transfer of \*O species, we performed <sup>18</sup>O-isotope labeling experiments. Because labeled CO<sub>2</sub> can lead to ambiguity from residual adsorption or desorption of <sup>18</sup>O-containing species, we



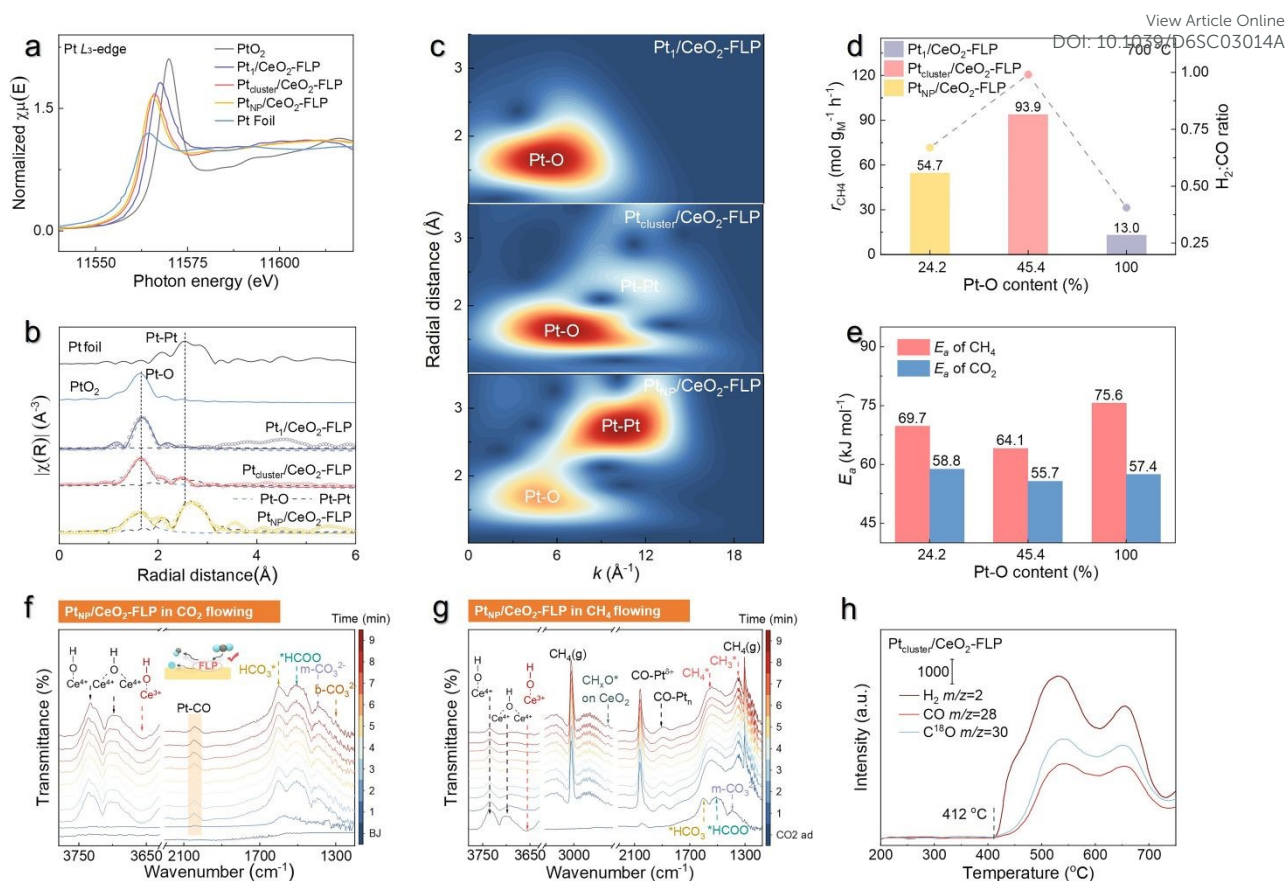


**Figure 4. Investigation on the functions of Pt clusters.** (a) XANES spectra of the Pt foil, Pt<sub>cluster</sub>/CeO<sub>2</sub>-FLP, Pt<sub>1</sub>/CeO<sub>2</sub>-FLP, Pt<sub>NP</sub>/CeO<sub>2</sub>-FLP and PtO<sub>2</sub>. (b) The k<sup>3</sup> weighted Fourier-transformed spectra derived from the EXAFS spectra. (c) Wavelet-transform plots by using k<sup>3</sup> space. (d) Direct correlation between Pt-O bond contents and CH<sub>4</sub> conversion rates/H<sub>2</sub>:CO ratios. (e) Plots of Pt-O bond contents vs. calculated E<sub>a</sub> values of Pt<sub>cluster</sub>/CeO<sub>2</sub>-FLP, Pt<sub>1</sub>/CeO<sub>2</sub>-FLP, Pt<sub>NP</sub>/CeO<sub>2</sub>-FLP for DRM. *In situ* DRIFTS spectra of Pt<sub>NP</sub>/CeO<sub>2</sub>-FLP under the (f) CO<sub>2</sub> flow and (g) CH<sub>4</sub> flow after CO<sub>2</sub> flow. Note: All of catalysts were pre-treated by a flow of Ar for 30 min. Then, a flow of 50 vol.% CO<sub>2</sub>/Ar was introduced and the DRIFTS signals were collected at 350 °C every 1 min. Subsequently, the 50 vol.% CO<sub>2</sub>/Ar gas was switched to a flow of 50 vol.% CH<sub>4</sub>/Ar. The DRIFTS signals were further collected at 350 °C every 1 min. (h) *In situ* mass spectrometry analysis of the temperature-programmed CH<sub>4</sub> oxidation of Pt<sub>cluster</sub>/CeO<sub>2</sub>-FLP with the pre-treatment by H<sub>2</sub><sup>18</sup>O.

designed the experiment using H<sub>2</sub><sup>18</sup>O pretreatment, which readily dissociates on CeO<sub>2</sub> but not on Pt clusters.<sup>32, 45, 46</sup> Specifically, after pretreating Pt<sub>cluster</sub>/CeO<sub>2</sub>-FLP with H<sub>2</sub><sup>18</sup>O at 150 °C for 30 min, then purging with Ar for 30 min to remove physically adsorbed species. The programmed temperature increase of CH<sub>4</sub> oxidation from 200 °C to 750 °C (10 vol.% CH<sub>4</sub>/He, 50 mL min<sup>-1</sup>) revealed the appearance of C<sup>18</sup>O/CO signal (Figure 4h), which directly demonstrated that \*O species stored in the CeO<sub>2</sub>-FLP support participate in CH<sub>4</sub> oxidation through oxygen transfer to Pt clusters. Furthermore, the H<sub>2</sub> signal appears simultaneously with the CO/C<sup>18</sup>O signals, indicating that CH<sub>4</sub> dissociates on Pt sites, with CO and H<sub>2</sub> formation. Notably, the observed C<sup>18</sup>O signal indicates that the oxygen involved in CH<sub>4</sub> oxidation originated predominantly from H<sub>2</sub><sup>18</sup>O-derived \*<sup>18</sup>O species stored in the CeO<sub>2</sub>-FLP support rather than from the lattice oxygen. Together, these results strongly support a spatially decoupled reaction pathway in which \*O migration couples CO<sub>2</sub> reduction on the support with CH<sub>4</sub> oxidation on Pt clusters.

**Activity matching between Pt clusters and FLP sites.** Achieving activity balance between the spatially decoupled CO<sub>2</sub> reduction and CH<sub>4</sub> oxidation is critical for highly performed DRM under the \*O

migration coupling process, as it ensures near stoichiometric H<sub>2</sub>:CO ratios (1:1) and long-term catalytic stability. As shown in Figure 5a, this activity balance is inherently determined by the quantitative relationship between FLP sites (responsible for CO<sub>2</sub> reduction) and Pt clusters (mediating CH<sub>4</sub> oxidation). While the FLP sites remain fixed within the CeO<sub>2</sub>-FLP supports, we precisely adjusted the number of Pt centers through controlling the Pt loadings. HAADF-STEM images revealed that increasing Pt loadings from 0.5 wt.% to 2.0 wt.% enhanced the densities of Pt clusters while preserving their similar cluster dimensions (an average diameter of 0.9~1.0 nm, Figure S23). This controlled variation in Pt cluster population enabled systematic modulation of the FLP-to-Pt site ratios, a crucial factor governing overall DRM performance.

For DRM, Pt loading significantly influenced reaction kinetics and product stoichiometry. At 0.5 wt.% Pt loading, the CH<sub>4</sub> conversion rate of 115.7 mmol g<sub>cat</sub><sup>-1</sup> h<sup>-1</sup> was lower than the CO<sub>2</sub> conversion rate of 169.7 mmol g<sub>cat</sub><sup>-1</sup> h<sup>-1</sup>, resulting in a significantly reduced H<sub>2</sub>:CO ratio of 0.81 at 700 °C (Figure 5b and S24). Elevating the Pt loading to 1 wt.%, accompanied with a higher density of Pt clusters, drastically improved the enhanced CH<sub>4</sub> conversion rate



**Table 1.** Fitting results of EXAFS for Pt<sub>1</sub>/CeO<sub>2</sub>-FLP, Pt<sub>cluster</sub>/CeO<sub>2</sub>-FLP and Pt<sub>NP</sub>/CeO<sub>2</sub>-FLP<sup>a</sup>

View Article Online

DOI: 10.1039/D6SC03014A

Sample	Paths	N <sup>b</sup>	R(Å) <sup>c</sup>	σ <sup>2</sup> (×10 <sup>-3</sup> Å <sup>2</sup> ) <sup>d</sup>	S <sub>0</sub> <sup>2</sup>	E <sub>0</sub> (eV)	R factor
Pt foil	Pt-Pt	12.0	2.77	-	-	-	-
PtO <sub>2</sub>	Pt-O	6.0	2.07	-	-	-	-
Pt <sub>1</sub> /CeO <sub>2</sub> -FLP	Pt-O	3.4 ± 0.1	2.04 ± 0.07	5.2 ± 0.9	0.8	7.4	0.018
Pt <sub>cluster</sub> /CeO <sub>2</sub> -FLP	Pt-O	4.4 ± 0.4	2.07 ± 0.02	2.1 ± 0.2	0.8	8.5	0.012
	Pt-Pt	5.3 ± 0.5	2.82 ± 0.16	5.2 ± 0.1			
Pt <sub>NP</sub> /CeO <sub>2</sub> -FLP	Pt-O	3.0 ± 0.7	2.10 ± 0.03	7.0 ± 2.9	0.8	8.7	0.008
	Pt-Pt	9.4 ± 0.2	2.78 ± 0.14	5.8 ± 0.6			

<sup>a</sup> The data ranges used in the fit are  $2.0 \leq k \leq 13.0 \text{ \AA}^{-1}$  and  $1.2 \leq R \leq 3.5 \text{ \AA}$ , depend on the quality of data. The number of variable parameters is out of a total of independent data points. R-factors for these fittings are all below 0.02.

<sup>b</sup> Average coordination number. The half path length.

<sup>c</sup> The paths for Pt-O, Pt-Pt are from the crystal structure of PtO<sub>2</sub> (P6<sub>3</sub>mc), Pt (Fm-3m).

<sup>d</sup> Debye-Waller factor.

(405.4 mmol g<sub>cat</sub><sup>-1</sup> h<sup>-1</sup>), matching the CO<sub>2</sub> conversion rate of 405.6 mmol g<sub>cat</sub><sup>-1</sup> h<sup>-1</sup>. Simultaneously, the H<sub>2</sub>:CO ratio approached 0.99, nearly achieving a stoichiometric ratio of 1 (Figure 5b). Therefore, increasing the Pt loading facilitated the optimal matching between Pt clusters and FLP sites.

Further increasing the Pt loading to 2 wt.% resulted in CH<sub>4</sub> and CO<sub>2</sub> conversion rates similar to those observed for Pt<sub>cluster</sub>/CeO<sub>2</sub>-FLP with 1 wt.% Pt loading (Figure 5b and S24). This observation demonstrated that the CH<sub>4</sub> activation and conversion depended on the migration of \*O species generated from the CO<sub>2</sub> reduction on FLP of CeO<sub>2</sub>-FLP, rather than the availability of Pt clusters. Consequently, CH<sub>4</sub> conversion rates plateau at the 1 wt.% Pt loading, as additional Pt clusters cannot compensate for the limited \*O supply from FLP. The extra CH<sub>4</sub> conversion would lead to carbon deposition on the catalyst surface (Figure 5a). Carbon balance analysis before and after the reaction revealed greater carbon imbalance for Pt<sub>cluster</sub>/CeO<sub>2</sub>-FLP with higher Pt loadings, indicating direct carbonization of CH<sub>4</sub> on Pt (Figure S25). Raman spectroscopy of the spent Pt<sub>cluster</sub>/CeO<sub>2</sub>-FLP catalysts proved the direct evidence of carbonaceous species (Figure S26). After 45 h reaction at 700 °C, thermogravimetric analysis (TGA) quantified carbon deposition rate of 2.69 mg g<sub>cat</sub><sup>-1</sup> h<sup>-1</sup> for the 2 wt.% Pt<sub>cluster</sub>/CeO<sub>2</sub>-FLP catalysts, which was ~7 times higher than that for 1 wt.% and 0.5 wt.% catalysts (0.39 and 0.38 mg g<sub>cat</sub><sup>-1</sup> h<sup>-1</sup>, Figure S27). Collectively, these results reveal the critical role of the balanced FLP-to-Pt site ratios in achieving efficient DRM performance with stoichiometric H<sub>2</sub>:CO output.

Kinetic analysis further clarified the activity matching requirements between Pt clusters and FLP sites (Figure S28). The comparable E<sub>0</sub> values of Pt<sub>cluster</sub>/CeO<sub>2</sub>-FLP for CO<sub>2</sub> conversion indicated that CO<sub>2</sub> adsorption and transformation predominantly occurred on FLP sites (Figure 5c). Theoretically, similar Pt clusters in Pt<sub>cluster</sub>/CeO<sub>2</sub>-FLP should yield comparable E<sub>0</sub> values for CH<sub>4</sub> conversion. However, when the Pt loading was 0.5 wt.%, the relatively large distance between Pt clusters and FLP sites resulted in a higher E<sub>0</sub> value for CH<sub>4</sub> conversion. In contrast, sufficient Pt loading (>1.0 wt.%) reduces the average spatial distance between Pt clusters and FLP sites, leading to sufficient migration and supply of \*O species and thus delivering comparable E<sub>0</sub> values for CH<sub>4</sub> conversion. When the number of Pt clusters matched that of FLP sites, the E<sub>0</sub> values for CH<sub>4</sub> conversion and CO<sub>2</sub> conversion were also comparable, thereby

facilitating the DRM reaction with near-stoichiometric ratio of H<sub>2</sub>:CO ≈ 1. This kinetic deconvolution highlights the critical roles of the available Pt clusters and FLP sites in balancing \*O supply (from FLPs) and CH<sub>4</sub> activation (at Pt) for DRM.

The CO<sub>2</sub> pulse experiments revealed that Pt<sub>cluster</sub>/CeO<sub>2</sub>-FLP with varying Pt loadings exhibited comparable \*O storage capacities (0.129-0.136 mmol g<sub>cat</sub><sup>-1</sup>, Figure 5d). These findings further confirm that FLP sites act as active centers for CO<sub>2</sub> reduction, generating reactive \*O species that subsequently participate in CH<sub>4</sub> oxidation pathways. Specially, the Pt loading of 0.5 wt.% yield a low rate of 0.043 mmol g<sub>cat</sub><sup>-1</sup> due to the insufficient amount and density of Pt clusters. When the Pt loadings were elevated to 1.0 wt.% and 2.0 wt.%, the CH<sub>4</sub> consumptions increased to 0.129 mmol g<sub>cat</sub><sup>-1</sup> and 0.138 mmol g<sub>cat</sub><sup>-1</sup>, respectively. Excessive Pt loading did not enhance DRM activity, as the FLP sites imposed a kinetic bottleneck of the \*O supply from the CO<sub>2</sub> reduction.

Notably, the observed CH<sub>4</sub> consumption over Pt<sub>cluster</sub>/CeO<sub>2</sub>-FLP did not scale with the population of Pt clusters as the Pt loading increased from 1.0 wt.% to 2.0 wt.%, contradicting the scenario where only interfacial oxygen is involved in the reaction. This deviation indicates that the \*O species are not confined to the Pt-CeO<sub>2</sub> interface. Instead, the facile migration of oxygen across the CeO<sub>2</sub>-FLP support enables the entire oxygen reservoir of the carrier to participate in CH<sub>4</sub> oxidation. Consequently, these findings further demonstrate that CO<sub>2</sub> activation occurs extensively on the FLP sites of CeO<sub>2</sub>-FLP, thereby achieving spatial decoupling from CH<sub>4</sub> oxidation at the Pt clusters.

Additionally, the optimal synergy of Pt clusters and FLP sites directly enhances catalytic stability. Pt<sub>cluster</sub>/CeO<sub>2</sub>-O<sub>v</sub>, lacking FLP sites, exhibited inferior stability, as evidenced by the substantially declined conversions of CH<sub>4</sub> and CO<sub>2</sub> during a period of 45 h (Figure 5e). Similarly, Pt<sub>cluster</sub>/CeO<sub>2</sub>-FLP with either insufficient (0.5 wt.%) or excessive (2.0 wt.%) Pt loading exhibited compromised durability, attributable respectively to limited CH<sub>4</sub> activation capacity and inadequate \*O-migration kinetics. In contrast, the optimally matched Pt<sub>cluster</sub>/CeO<sub>2</sub>-FLP (1 wt.% Pt loading) catalyst delivered exceptional long-term stability, maintaining nearly constant CH<sub>4</sub> conversion rates (Figure 5e) and near-stoichiometric H<sub>2</sub>:CO ratio (Figure S29) for over 400 h. During the initial 100 h, when the H<sub>2</sub>/CO ratio



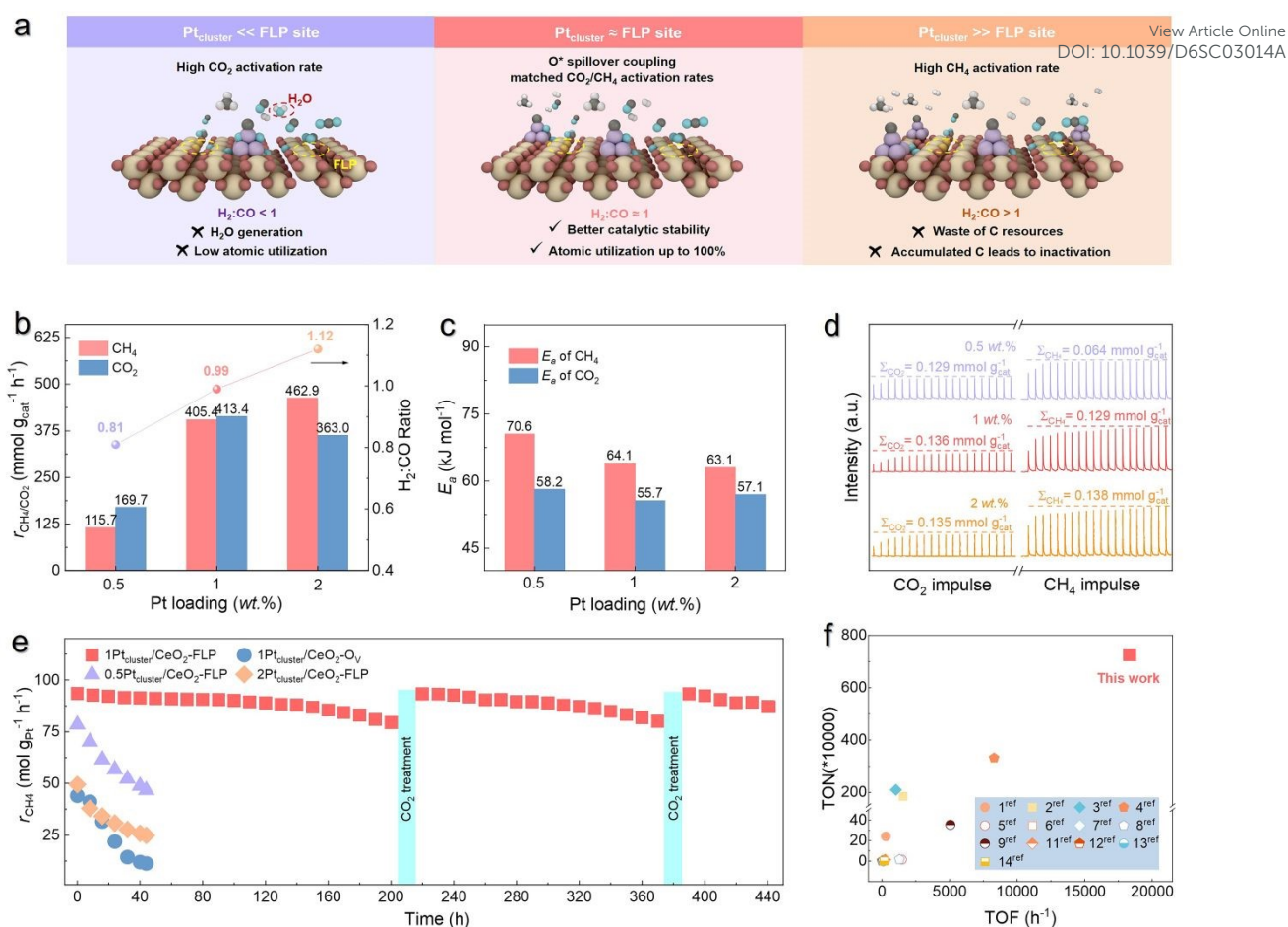


**Figure 5. Activity matching.** (a) Scheme of activity matching between Pt clusters and FLPs for reaction. (b) Influences of Pt loadings on the CH<sub>4</sub>/CO<sub>2</sub> generation rates and H<sub>2</sub>:CO ratios of the Pt<sub>cluster</sub>/CeO<sub>2</sub>-FLP catalysts for DRM. (c) Influence of Pt loadings on the E<sub>a</sub> values of Pt<sub>cluster</sub>/CeO<sub>2</sub>-FLP for CO<sub>2</sub> and CH<sub>4</sub> conversions. (d) Pulsed reactions of CO<sub>2</sub> and CH<sub>4</sub> over Pt<sub>cluster</sub>/CeO<sub>2</sub>-FLP with various Pt loadings. (e) Catalytic stability of various catalysts with a WHSV of 30,000 mL g<sub>cat</sub><sup>-1</sup> h<sup>-1</sup> (CH<sub>4</sub>:CO<sub>2</sub>:N<sub>2</sub>=2:2:1) at 700 °C. CO<sub>2</sub> treatment conditions: CO<sub>2</sub>/N<sub>2</sub> at 700°C for 10 h with a WHSV of 18,000 mL g<sub>cat</sub><sup>-1</sup> h<sup>-1</sup>. (f) Comparison of TON and TOF between Pt<sub>cluster</sub>/CeO<sub>2</sub>-FLP and other state-of-the-art catalysts under similar reaction conditions (See Table S2 for more details).

remained near 1, no detectable water appeared in the product stream, indicating effective suppression of the RWGS reaction. However, XPS analysis of the spent Pt<sub>cluster</sub>/CeO<sub>2</sub>-FLP catalyst revealed both reduced surface defect and accumulated carbonaceous species (Figure S30), which together mask Pt clusters and FLP sites. Notably, a slight 15% loss in activity during long-term testing was completely reversed by a simple CO<sub>2</sub> treatment (Figure 5e). This remarkable stability reflected in a turnover number (TON) exceeding 7,200,000 per exposed Pt site for CH<sub>4</sub> conversion (Figure 5f and S31). To the best of our knowledge, Pt<sub>cluster</sub>/CeO<sub>2</sub>-FLP represents the first to simultaneously achieve such a record-high TON and unprecedented activity, with its TON value nearly doubling the previously reported maximum (Figure 5f).

Finally, we propose a catalytic process for DRM on Pt<sub>cluster</sub>/CeO<sub>2</sub>-FLP that spatially decouples CO<sub>2</sub> reduction and CH<sub>4</sub> oxidation, as illustrated in Figure 1c. The CO<sub>2</sub> reduction step follows a Mars-van Krevelen (MvK) mechanism: CO<sub>2</sub> is adsorbed and activated at FLP sites, directly forming CO and leaving \*O species on the CeO<sub>2</sub>-FLP support. Subsequently, the \*O species migrate from FLP sites to Pt clusters. On Pt clusters, CH<sub>4</sub> is converted to CO and H<sub>2</sub>

via \*CH<sub>x</sub>O intermediates, facilitated by the migrated \*O species. Thus, while the individual CO<sub>2</sub> reduction step obeys the classical MvK redox cycle, the overall process represents a modified MvK-type pathway enabled by spatial decoupling and \*O migration between distinct active sites. This design separates CO<sub>2</sub> reduction (FLP sites) from CH<sub>4</sub> oxidation (Pt clusters) and couples them through oxygen spillover. Through precise matching of Pt clusters and FLP sites, the two half-reactions are efficiently coupled, leading to a near-stoichiometric H<sub>2</sub>/CO ratio and sustained DRM activity.

## Conclusions

In summary, this work demonstrates that \*O migration across a spatially decoupled Pt/CeO<sub>2</sub> catalyst enables near-stoichiometric DRM under continuous operation, delivering durable and high-performance DRM catalysis with a stoichiometric H<sub>2</sub>:CO ratio. This catalyst separates the antagonistic adsorption and activation steps: CO<sub>2</sub> is selectively reduced at FLP sites on the CeO<sub>2</sub>(110) facet, while CH<sub>4</sub> is partially oxidized on Pt clusters, with \*O shuttling dynamically between the two sites. This \*O-transport mechanism



intrinsically couples the two half-reactions, maintains a balanced redox cycle, and effectively maintains a H<sub>2</sub>:CO ratio of 0.99 while suppressing coke formation and deactivation pathways. As a result, the catalyst delivers a record CH<sub>4</sub> conversion rate of 93.9 mol g<sub>Pt</sub><sup>-1</sup> h<sup>-1</sup> at 700 °C with stable operation exceeding 400 h under continuous, isothermal conditions. Although the present study employs Pt/CeO<sub>2</sub>(110) as a model platform, the underlying principle is not limited to this specific combination. The key requirements are: (i) a reducible oxide support capable of forming FLP sites (adjacent oxygen vacancies) that strongly activate CO<sub>2</sub>, and (ii) metal sites (clusters or nanoparticles) that can activate CH<sub>4</sub> and accept migrating \*O species. Many earth-abundant metals (e.g., Ni, Co, Ru) and other reducible oxides (e.g., TiO<sub>2</sub>, WO<sub>3</sub>, In<sub>2</sub>O<sub>3</sub>) are known to exhibit similar oxygen spillover behavior and have been reported to form frustrated Lewis pair-like defects under reducing conditions. Therefore, we anticipate that the spatial decoupling strategy can be extended to more practical catalyst compositions, guided by the design principles established here.

### Author contributions

W. L. performed most of the experiments. J. Y., W. G. and Q. G. participated in data analysis. S. Z. and Y. Q. designed the studies and wrote the paper. All authors discussed the results and commented on the manuscript.

### Conflicts of interest

There are no conflicts to declare.

### Data availability

Data will be made available on request.

### Acknowledgements

This work was supported by National Natural Science Foundation of China Young Student Basic Research Project (Doctoral Student) (225B2209), and the Key Projects of Natural Science Basic Research Program of Shannxi Province (2024JC-TBZC-16).

### Notes and references

1. Intelligence, M. Syngas Market Size. Mordor Intelligence <https://www.mordorintelligence.com/industry-reports/syngas-market> (accessed 07 July 2025).
2. C. Palmer, D. C. Upham, S. Smart, M. J. Gordon, H. Metiu and E. W. McFarland, *Nat. Catal.*, 2020, **3**, 83-89.
3. Q. Zhu, H. Zhou, L. Wang, L. Wang, C. Wang, H. Wang, W. Fang, M. He, Q. Wu and F.-S. Xiao, *Nat. Catal.*, 2022, **5**, 1030-1037.
4. Y. Song, E. Ozdemir, S. Ramesh, A. Adishev, S. Subramanian, A. Harale, M. Albuali, B. A. Fadhel, A. Jamal, D. Moon, S. H. Choi and C. T. Yavuz, *Science*, 2020, **367**, 777-781.
5. Y. Liu, D. Deng and X. Bao, *Chem*, 2020, **6**, 2497-2514.
6. L. Zhou, J. M. P. Martinez, J. Finzel, C. Zhang, D. F. Swearer, S. Tian, H. Robotjazi, M. Lou, L. Dong, L. Henderson, P. Christopher, E. A. Carter, P. Nordlander and N. J. Halas, *Nat. Energy*, 2020, **5**, 61-70.
7. T. Zhou, X. Li, J. Zhao, L. Luo, Y. Wang, Z. Xiao, S. Hu, R. Wang, Z. Zhao, C. Liu, W. Wu, H. Li, Z. Zhang, L. Zhao, H. Yan and J. Zeng, *Nat. Mater.*, 2025, **24**, 891-899.
8. S. D. Senanayake, J. A. Rodriguez and J. F. Weaver, *Acc. Chem. Res.*, 2020, **53**, 1488-1497.
9. D. Pakhare and J. Spivey, *Chem. Soc. Rev.*, 2014, **43**, 7813-7837.
10. M.-M. Millet, G. Algara-Siller, S. Wrabetz, A. Mazheika, F. Girgsdies, D. Teschner, F. Seitz, A. Tarasov, S. V. Levchenko, R. Schlögl and E. Frei, *J. Am. Chem. Soc.*, 2019, **141**, 2451-2461.
11. L. Sandoval-Diaz, D. Cruz, M. Vuijk, G. Ducci, M. Hävecker, W. Jiang, M. Plodinec, A. Hammud, D. Ivanov, T. Götsch, K. Reuter, R. Schlögl, C. Scheurer, A. Knop-Gericke and T. Lunkenbein, *Nat. Catal.*, 2024, **7**, 161-171.
12. M. Akri, S. Zhao, X. Li, K. Zang, A. F. Lee, M. A. Isaacs, W. Xi, Y. Gangarajula, J. Luo, Y. Ren, Y. T. Cui, L. Li, Y. Su, X. Pan, W. Wen, Y. Pan, K. Wilson, L. Li, B. Qiao, H. Ishii, Y. F. Liao, A. Wang, X. Wang and T. Zhang, *Nat. Commun.*, 2019, **10**, 5181.
13. H. Wang, G. Cui, H. Lu, Z. Li, L. Wang, H. Meng, J. Li, H. Yan, Y. Yang and M. Wei, *Nat. Commun.*, 2024, **15**, 3765.
14. Q. Zhu, H. Zhou, L. Wang, L. Wang, C. Wang, H. Wang, W. Fang, M. He, Q. Wu and F.-S. Xiao, *Nat. Catal.*, 2022, **5**, 1030-1037.
15. Y. Tang, Y. Wei, Z. Wang, S. Zhang, Y. Li, L. Nguyen, Y. Li, Y. Zhou, W. Shen, F. F. Tao and P. Hu, *J. Am. Chem. Soc.*, 2019, **141**, 7283-7293.
16. C. Palmer, D. C. Upham, S. Smart, M. J. Gordon, H. Metiu and E. W. McFarland, *Nat. Catal.*, 2020, **3**, 83-89.
17. H. Lv, X. Dong, R. Li, C. Zeng, X. Zhang, Y. Song, H. Liu, J. Shao, N. Ta, Q. Zhao, Q. Fu, J. Xiao, G. Wang and X. Bao, *Nat. Chem.*, 2025, **17**, 695-702.
18. L. C. Buelens, V. V. Galvita, H. Poelman, C. Detavernier and G. B. Marin, *Science*, 2016, **354**, 449-452.
19. L. Zeng, Z. Cheng, J. A. Fan, L.-S. Fan and J. Gong, *Nat. Rev. Chem.*, 2018, **2**, 349-364.
20. X. Zhang, Y. Xu, Y. Liu, L. Niu, Y. Diao, Z. Gao, B. Chen, J. Xie, M. Bi, M. Wang, D. Xiao, D. Ma and C. Shi, *Chem*, 2023, **9**, 102-116.
21. S. Zhang, Z. Q. Huang, Y. Ma, W. Gao, J. Li, F. Cao, L. Li, C. R. Chang and Y. Qu, *Nat. Commun.*, 2017, **8**, 15266.
22. T. Montini, M. Melchionna, M. Monai and P. Fornasiero, *Chem. Rev.*, 2016, **116**, 5987-6041.
23. S. Zhang, Z. Tian, Y. Ma and Y. Qu, *ACS Catal.*, 2023, **13**, 4629-4645.
24. J. Graciani, K. Mudiyansele, F. Xu, A. E. Baber, J. Evans, S. D. Senanayake, D. J. Stacchiola, P. Liu, J. Hrbek, J. F. Sanz and J. A. Rodriguez, *Science*, 2014, **345**, 546-550.
25. Z. Liang, T. Li, M. Kim, A. Asthagiri and J. F. Weaver, *Science*, 2017, **356**, 299-303.
26. Q. Cheng, X. Yao, L. Ou, Z. Hu, L. Zheng, G. Li, N. Morlanes, J. L. Cerrillo, P. Castano, X. Li, J. Gascon and Y. Han, *J. Am. Chem. Soc.*, 2023, **145**, 25109-25119.
27. Z. Rao, K. Wang, Y. Cao, Y. Feng, Z. Huang, Y. Chen, S. Wei, L. Liu, Z. Gong, Y. Cui, L. Li, X. Tu, D. Ma and Y. Zhou, *J. Am. Chem. Soc.*, 2023, **145**, 24625-24635.
28. M. Filez, V. De Coster, H. Poelman, V. Briois, A. Beauvois, J. Dendooven, M. B. J. Roeffaers, V. Galvita and C. Detavernier, *Nat. Catal.*, 2025, **8**, 187-195.
29. S. Kattel, P. Liu and J. G. Chen, *J. Am. Chem. Soc.*, 2017, **139**, 9739-9754.



## ARTICLE

## Journal Name

30. S. Navarro-Jaén, M. Virginie, J. Bonin, M. Robert, R. Wojcieszak and A. Y. Khodakov, *Nat. Rev. Chem.*, 2021, **5**, 546-579.
31. R. Ye, J. Ding, T. R. Reina, M. S. Duyar, H. Li, W. Luo, R. Zhang, M. Fan, G. Feng, J. Sun and J. Liu, *Nat. Synth.*, 2025, **4**, 288-302.
32. S. Zhang, Y. Liu, M. Zhang, Y. Ma, J. Hu and Y. Qu, *Nat. Commun.*, 2022, **13**, 5527.
33. S. Zhang, Z. Xia, Y. Zou, F. Cao, Y. Liu, Y. Ma and Y. Qu, *J. Am. Chem. Soc.*, 2019, **141**, 11353-11357.
34. J. Ren, Y. Liu, Y. Wang, W. Guo, K. Ma, Y. Qu and S. Zhang, *ACS Nano*, 2026, **20**, 4470-4478.
35. E. Garand, T. Wende, D. J. Goebbert, R. Bergmann, G. Meijer, D. M. Neumark and K. R. Asmis, *J. Am. Chem. Soc.*, 2010, **132**, 849-856.
36. S. M. Jin, C. Kwon, A. Bugaev, B. Karakurt, Y. C. Lin, L. Savereide, L. P. Zhong, V. Boureau, O. Safonova, S. Kim and J. S. Luterbacher, *Nat. Catal.*, 2024, 1119-1212.
37. C. Vogt, E. Groeneveld, G. Kamsma, M. Nachtegaal, L. Lu, C. J. Kiely, P. H. Berben, F. Meirer and B. M. Weckhuysen, *Nat. Catal.*, 2018, **1**, 127-134.
38. W. Li, J. Gan, Y. Liu, Y. Zou, S. Zhang and Y. Qu, *Angew. Chem. Int. Ed.*, 2023, **62**, e202305661.
39. L. F. Bobadilla, J. L. Santos, S. Ivanova, J. A. Odriozola and A. Urakawa, *ACS Catal.*, 2018, **8**, 7455-7467.
40. H. Shen, Y. Dong, S. Yang, Y. He, Q. Wang, Y. Cao, W. Wang, T. Wang, Q. Zhang and H. Zhang, *Nano Res.*, 2022, **15**, 5831-5841.
41. W. Li, B. Liu, Q. Guo, W. Guo, S. Zhang and Y. Qu, *Nat. Commun.*, 2025, **16**, 7335.
42. F. Xue, C. Zhang, C. Cheng, X. Yan, F. Liu, X. Liu, B. Jiang, Q. Zhang, L. Sun, H. Peng, W. H. Huang, C. W. Pao, Z. Hu, M. Chen, D. Su, M. Liu, X. Huang and Y. Xu, *Nat. Commun.*, 2024, **15**, 10451.
43. J. Ma, C. Zhu, K. Mao, W. Jiang, J. Low, D. Duan, H. Ju, D. Liu, K. Wang, Y. Zang, S. Chen, H. Zhang, Z. Qi, R. Long, Z. Liu, L. Song and Y. Xiong, *Nat. Commun.*, 2023, **14**, 1410.
44. J. F. Weaver, C. Hakanoglu, A. Antony and A. Asthagiri, *Chem. Sev. Rev.*, 2014, **43**, 7536-7547.
45. Q. Fu, H. Saltsburg and M. Flytzani-Stephanopoulos, *Science*, 2003, **301**, 935-938.
46. K. Ding, A. Gulec, A. M. Johnson, N. M. Schweitzer, G. D. Stucky, L. D. Marks and P. C. Stair, *Science*, 2015, **350**, 189-192.

View Article Online  
DOI: 10.1039/D6SC03014A

Open Access Article. Published on 01 June 2026. Downloaded on 6/3/2026 11:50:14 PM.  
This article is licensed under a Creative Commons Attribution 3.0 Unported Licence.



Chemical Science Accepted Manuscript

### Data Availability Statement

The authors declare that the main data supporting the findings are available within the article and supplementary information from the corresponding author upon request.

